Inkjet Printing of Single-Crystalline Bi₂Te₃ Thermoelectric Nanowire Networks

Bolin Chen, Suprem R. Das, Wei Zheng, Bowen Zhu, Biao Xu, Sungbum Hong, Chenghan Sun, Xinwei Wang, Yue Wu, and Jonathan C. Claussen*

Large-scale and low-cost fabrication techniques are needed to commercialize highly efficient, nanomaterial-based thermoelectric generators (TEGs) for use in small-scale, flexible applications (e.g., wearable energy harvesters). This study presents the first demonstration of inkjet-printed networks of phase-pure, single-crystalline Bi_2Te_3 thermoelectric nanowires (BTNWs) that are amenable to large-scale production. The BTNWs are synthesized via chemical batch processing and formulated into a jettable ink that is printed onto glass substrates and subsequently annealed in nitrogen and forming gas environments. The inkjet-printed BTNWs annealed in forming gas provide the most favorable results with comparable thermoelectric performances to bulk Bi_2Te_3 materials (Seebeck coefficient up to 140 μV K^{-1}) while approximately utilizing only 1% to 3% of the telluride materials found in their bulk counterparts. Thus, these printed BTNWs help pave the way for the development of low-cost and scalable TEGs.

1. Introduction

Thermoelectric generators (TEGs), solid state devices that convert heat into electricity, have been in use for over 35 years in primarily large-scale applications such as power plants and space exploration equipment (e.g., NASA's space probe Voyager).[1,2] Recent efforts to increase the efficiency of thermoelectric materials via nanoscale synthesis and structuring have begun to enable small-scale TEG applications including those associated with flexible and wearable platforms such as TEG-embedded T-shirts and armbands.[3–5] Nanoscale bismuth chalcogenide (e.g., bismuth telluride (Bi_2Te_3), its doped derivatives, and bismuth selenide (Bi_2Se_3)) have shown great potential for use in small-scale TEG applications as they are among the most efficient materials for thermoelectric power generation (the figure of merit or *ZT* values ranging between 0.8 and 1.0 for bulk at low temperature ranges, i.e., 200–400 K).[6–8] Furthermore, the synthesis of Bi_2Te_3 materials in the form of nanowires has led to further increases in *ZT* values due to reduced thermal conductivities pertaining to surface and boundary phonon scattering, enhanced Seebeck coefficients due to quantum confinement of carriers, and 1D carrier transport due to quantized density of states.[9–11] Thus, Bi_2Te_3 thermoelectric nanowires (BTNWs) show tremendous promise for the development of small-scale TEGs.

Numerous techniques have been developed for incorporating BTNWs into TEGs. For example, phase pure and crystalline BTNWs (average diameter ≈30–40 nm and average length ≈500 nm; see Figure S1 in the Supporting Information) have been synthesized and formed into macroscale pellets via hot-pressing techniques.[12–14] These nanowire-infused pellets display several advantages over bulk material pellets including enhanced phonon scattering due to the high degree of grain boundaries/nanowire interfaces, high electrical conductivity (423–507 S cm^{-1}), and high Seebeck coefficients (240–360 μV K^{-1}).[12] These bulk composite pellets can be further processed into millimeter-thick pillar device structures via compressing/sintering, micromachining, and manual welding metal interconnects—techniques that are labor intensive and require copious amounts of expensive, scarce, and sometimes toxic telluride-based nanomaterial. Other research groups have made tremendous strides on improving/tuning the properties of BTNWs.[15–17] However, this research is limited to lab-scale device fabrication and measurements performed on a single nanowire, thin film of nanocrystals, or on micron-scale heterostructures—techniques that are not amenable to large-scale TEG production.

Some research groups have begun to explore large-scale, thin-film fabrication of TEG devices. Physical vapor deposition of TEG materials (e.g., evaporation of both Bi and Te simutaneously from two distinct crucibles) within a low pressure/vacuum environment is costly as it requires high power to evaporate the metal and maintain the vacuum as well as highly trained personnel to operate the equipment. Other groups have developed high-yield, low-cost printing methods. For example, various printing techniques such as screen printing, and dispenser printing have been recently explored for producing TEGs in a scalable fashion.[7,18–20] However, screen printing has

B. Chen, Dr. S. R. Das, B. Zhu, Prof. X. Wang,
Prof. J. C. Claussen
Mechanical Engineering
Iowa State University
Ames, IA 50011, USA
E-mail: jcclauss@iastate.edu
W. Zheng, Dr. B. Xu, S. Hong, C. Sun, Prof. Y. Wu
Chemical and Biological Engineering
Iowa State University
Ames, IA 50011, USA

multiple drawbacks including low line resolution (>100 μm), material waste as material becomes adhered to the squeegee in lieu of being printed, and higher prototyping costs as a new stencil or mask is needed for each new design. Dispenser printing also has drawbacks such as the necessity to use viscous pastes (≈100—10 000 cP for dispenser printing vs 5–15 cP for inkjet printing) that require the use of additive materials (e.g., poly(3-hexyl thiophene)) and controlling the height and temperature of the dispenser needle while preventing breakage and contamination are all challenging the printing efficiency as well as overall cost.[21] Also both screen and dispenser printing produce thick films (i.e., >100 μm) that introduce a degree of parasitic resistances due to the higher number of junctions found in thicker printed materials.[22,23] However, high-resolution (<100 μm feature size) inkjet printing that requires no mask or stencil (i.e., printer can be programmed with computer-aided design software for pattern formation) and can print droplet thick lines (<1 μm) provides an alternative more precise and lower cost scalable printing process as shown in inkjet-printed electrochemical sensors,[24] transparent conductors,[25] photovoltaics,[26] and supercapacitors.[27]

Herein we report, for the first time, inkjet-printed BTNWs without any additives/conducting elements, for scalable, TEG production. The nanowires are synthesized via solution phase processing according to our previous protocols. The nanowires are converted into jettable ink, without the use of additives such as exogenous conductive particles, and printed into films of various thicknesses. The printed BTNW films are subsequently annealed within two distinct ambient conditions (i.e., nitrogen vs forming gas ambient) to improve their thermoelectric properties—electrical conductivity, thermal diffusivity, and Seebeck coefficient.

2. Results and Discussion

Batch synthesis of BTNWs was conducted following our previously reported chemical synthesis methods (**Figure 1**a and the Experimental Section).[12,13] In short, ultrathin tellurium nanowires were fabricated by dissolving and reducing a tellurium precursor (i.e., tellurium dioxide (TeO_2)) along with potassium hydroxide (KOH), polyvinylpyrrolidone (PVP), and ethylene glycol (EG) within a controlled temperature (160 °C) bath for 10 min. A small injection of hydrazine hydrate (≈1 mL) is added to the solution to help reduce TeO_2 and form tellurium nanowires. Next bismuth precursors ($BiNO_3$) were added to the mixture to induce the formation of the final BTNWs. Note that the PVP was used in the reaction to act as a surfactant that prevents nanowire amalgamation and proper nanowire formation.

The BTNWs were next made into a jettable ink and printed onto both rigid substrates (Figure 1b,c and the Experimental Section). After BTNW formation, the nanowires were washed via centrifugation, redispersed in Deionized (DI) water with the aid of bath sonication to form a jettable ink, and finally inkjet printed onto glass substrates for testing. Both the BTNW dispersion concentration and the solution viscosity (10–12 cP) were tuned to prevent the piezoelectric printer nozzle from clogging. It should be noted that the average nanowire length of the BTNWs is ≈1440 nm and average diameter is ≈30 nm, both of which are much smaller than the 1 pL nozzle diameter.[12,14] Therefore, additional size reduction processing of the BTNWs, such as ball milling, was unnecessary in the ink formulation process. The number of passes that the printer head made to complete the printer process was varied (i.e., 25 print layers ≈0.4 μm thick, 50 print layers ≈0.75 μm thick, 75 print layers ≈1.1 μm thick, and 100 print layers ≈1.6 μm thick) and
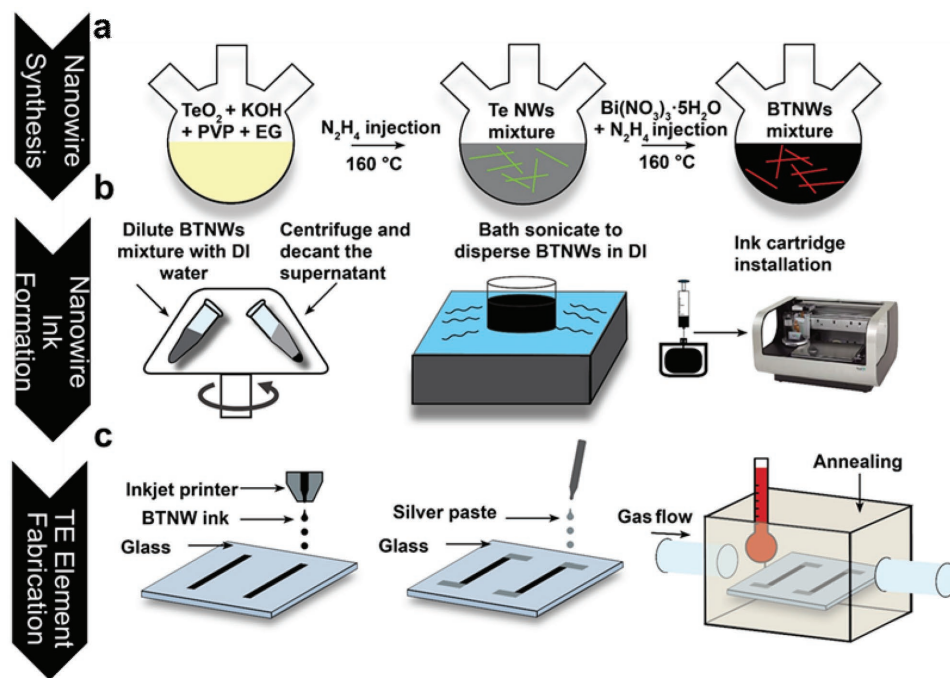
**Figure 1.** Schematic diagram of the nanowire synthesis, processing, and printing protocols: a) Two-step chemical synthesis of Bi_2Te_3 nanowires (BTNWs), b) BTNW ink formulation, and c) inkjet printing of resultant BTNW ink and post annealing processes.

ADVANCED
SCIENCE NEWS
www.advancedsciencenews.com

ADVANCED
ELECTRONIC
MATERIALS
www.advelectronicmat.de

FULL PAPER

the nozzle voltage was tuned (21–24 V) to subsequently alter the thickness of the printed BTNW layer/network and subsequently to improve its thermoelectric efficiency.

The thermoelectric properties of the printed BTNWs were also improved by using postprint annealing processing. Various techniques, including thermal annealing, have been used to reduce the interparticle resistance of 1D nanowire network structures comprised of a variety of materials including carbon nanotubes and silver nanowires.[28–32] In this work, we developed two distinct thermal annealing protocols for the printed BTNW networks: (1) thermal annealing in a purely nitrogen ambient and (2) thermal annealing in a forming gas ambient (i.e., 95% pure dry argon gas premixed with 5% pure dry hydrogen gas). Both annealing protocols were conducted at 400 °C for 2 h followed by a cooling time in the same respective gas. Field emission scanning electron microscopy (FESEM) images of the printed BTNW networks reveal morphological changes in the nanowire nanostructure before and after the annealing processes (**Figure 2**). The unannealed BTNWs retain their original 1D dimensions/morphology after the printing process with an approximate average length and width of 1.5 µm and 30 nm, respectively (Figure 2a and the Supporting Information). However, upon annealing in the forming gas ambient, morphological/density changes in the nanowires

occur with closer nanowire packing arrangements and thicker/shorter nanowires (approximate average length and width of 130 µm and 40 nm, respectively).

The crystal structure/phase information also varied according to the postprint BTNW annealing conditions. X-ray diffraction (XRD) measurements of unannealed and annealed printed BTNWs revealed changes in the crystallinity as noted in the indexed XRD peaks, i.e., (015), (1010), and (110) as denoted in **Figure 3**. These peaks correspond to the 2θ values that are consistent with Bi_2Te_3 material peaks while the sharpness of the peaks is an indicator of the crystallinity of the nanowires (i.e., an increase in the sharpness of the 2θ peaks signifies an increase in the crystalline nature of the nanowires). Also, it should be noted that the XRD 2θ broad peak, visible between 15° and 40° on all tested samples, is indicative of the substrate peak (amorphous nature of glass) upon which the BTNWs were printed on (see glass control XRD measurement in Figure 3). Comparison of XRD peak intensities reveals that the 2θ peaks become sharper after the printed BTNWs are annealed in a forming gas ambient as compared to BTNWs annealed in nitrogen or not annealed at all. The improved sharpness in XRD peaks in the case of forming gas annealed printed nanowires is attributed to the packed microstructure of the BTNW networks that also correspond to the visible morphological changes displayed in Figure 2 as well as the electrical and thermoelectric properties presented in the subsequent sections. However, the decreased intensity of XRD peaks in case of nitrogen-annealed nanowire films might arise from the enhanced anisotropy of the network causing incoherent X-ray scattering as compared to the unannealed sample. The presence of no other peaks found in the three samples indicates the phase purity of the material and denotes a contaminant-free BTNW environment
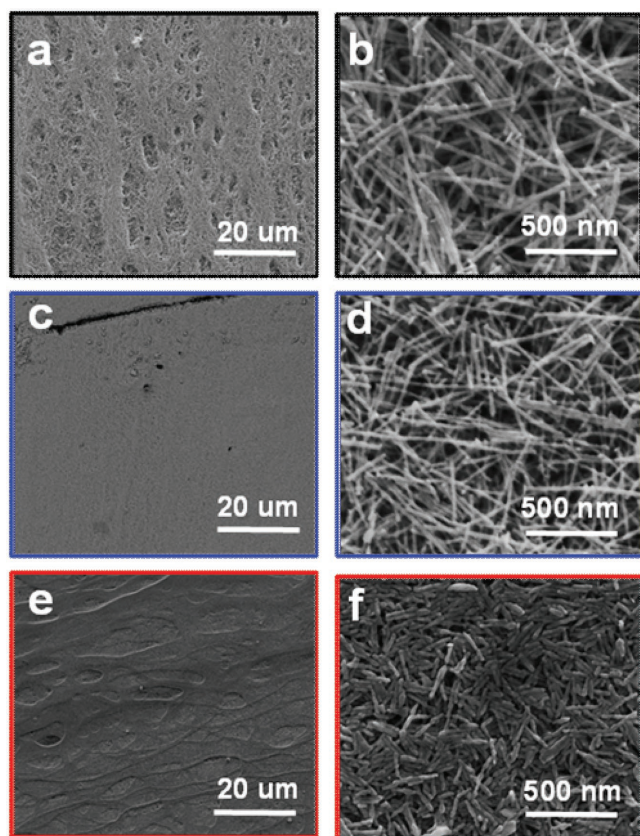
Figure 2. Low-resolution (left column) and high-resolution (right column) FESEM images of a,b) unannealed printed BTNWs nanowires, c,d) annealed in a nitrogen gas ambient, and e,f) annealed in a forming gas. All annealing was performed at 400 °C for 1 h duration.
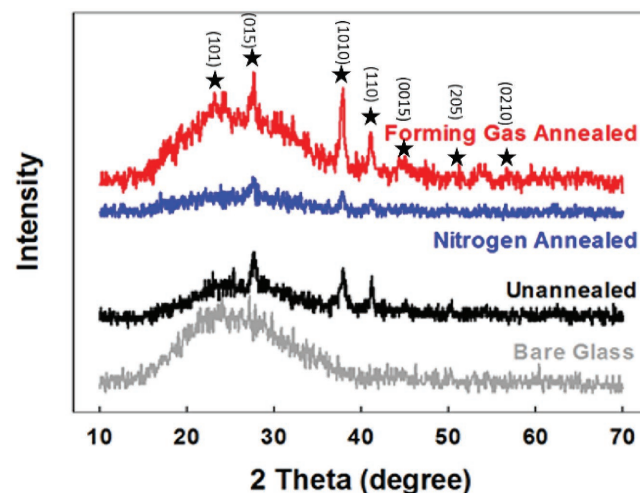

Figure 3. X-ray diffraction (XRD) measurements of bare glass substrate (gray), inkjet-printed BTNWs that are unannealed (black) and annealed in a nitrogen (blue) and forming gas (red) ambient, respectively. Sharp Bi_2Te_3 peaks (indexed) as well as the broad substrate peaks are portrayed while no impurity peaks are observed. The thickness of the printed BTNW networks corresponds to 100 printing passes (1.6 µm thick). As a reference, "*"symbols are shown to provide the position of the peaks and indices corresponding to a Bi_2Te_3 film.

without material segregation. Furthermore, energy dispersive X-ray spectroscopy measurements showed that all X-ray peaks correspond to either Bi or Te (see Section S2 in the Supporting Information).[12]

Thermal annealing, in general, plays an important role in network formation by providing input thermal excitation to the system and in rearranging the network geometry in an optimum manner. More importantly, a controlled annealing such as the ones used in the present work maintains oxidation-free nanomaterial processing, cleans the surfactants and surface of the nanowires, and introduces crystalline wire–wire nanojoints by forming active electronic conduction channels. Compared to annealing in a nitrogen ambient, a forming gas annealing provides additional electronic passivation of active defects (such as dangling bonds) present on the network. Moreover, the pronounced microstructure changes observed in forming gas annealing could arise from high-temperature annealing with exposure to high-energy hydrogen radicals. Next, the electrical conductivity of the printed BTNWs was acquired for networks annealed in nitrogen and forming gas ambient with varying thicknesses (i.e., 25 print layers ≈0.4 µm thick, 50 print layers ≈0.75 µm thick, 75 print layers ≈1.1 µm thick, and 100 print layers ≈1.6 µm thick; **Figure 4**a). The dependence of the room temperature electrical conductivity and thermal diffusivity of the distinctly annealed BTNW films on the thickness of the film is portrayed in Figure 4a,c. The film

with sparse NW density (corresponding to 25 printing passes) displayed an electrical conductivity of ≈800 –1200 S m^{-1}, a value that is roughly an order of magnitude smaller than recently reported metallic nanowire (i.e., silver nanowire) networks that were inkjet printed with comparable thickness.[33] The lower electrical conductivity of the printed BTNWs, as compared to the metallic nanowires, is most likely due to the higher energy gaps of semiconductor materials as compared to the overlapping Fermi levels associated with a conduction band of typical metallic materials. Also, the electrical conductivity of the BTNW network changes according to BTNW thickness or density as dictated by the number of printer passes used to create the networks (i.e., 50, 75, and 100 printer passes). For example, the electrical conductivity initially increases from ≈0.45 S m^{-1} × 10^3 to 0.75 S m^{-1} × 10^3 as the number of printer passes increases from 25 to 50 for the BTNWs annealed in forming gas, and then finally drops in electrical conductivity for printer pass thickness greater than 75 printer passes. The initial increase in electrical conductivity is most likely due to increased electrical pathways with increasing BTNW thickness. Finally, a saturation point is reached where the forming gas annealing process is no longer capable of penetrating the entire thickness of the film and unannealed underlying BTNWs that contain numerous intertrapped tube/tube connections that have not been passivated most likely increase the overall electrical resistance of the BTNW network. In contrast, for nitrogen-annealed printed
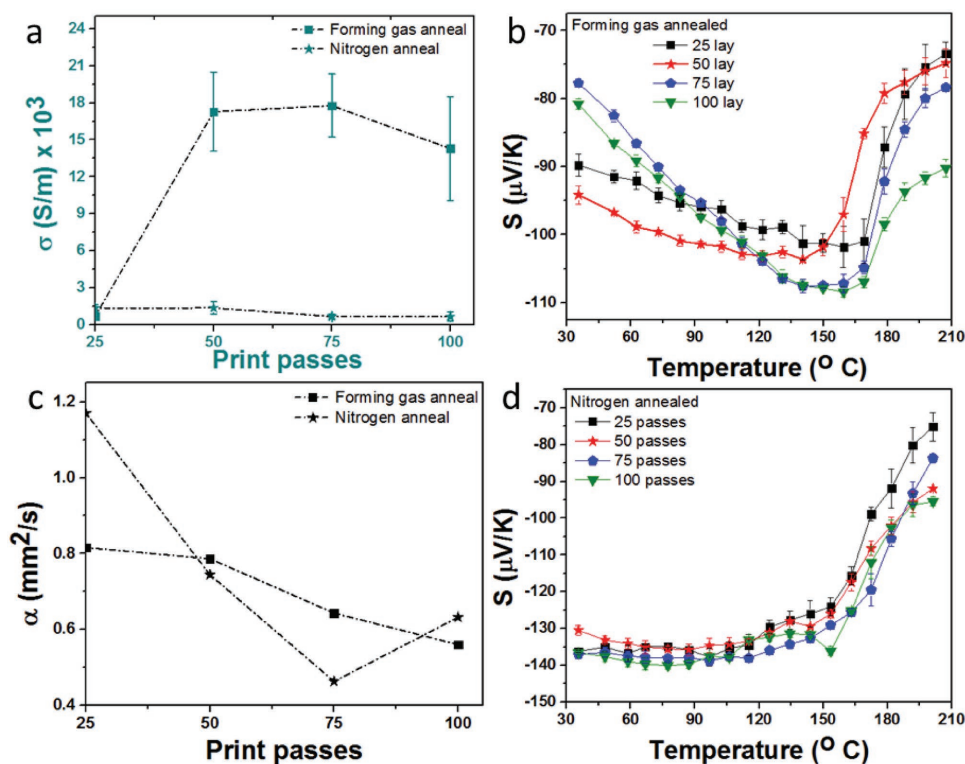
Figure 4. Room temperature electrical conductivity, room temperature thermal diffusivity, and temperature-dependent Seebeck coefficients of all eight printed films are shown; a,c) the electrical conductivity versus thickness and the thermal diffusivity versus thickness, respectively, of the printed BTNWs annealed in a forming gas and nitrogen gas ambient; b,d) the Seebeck coefficient of the printed BTNWs of varying thickness annealed in a forming gas and nitrogen gas ambient, respectively, measured at various temperatures (35–200 °C by increments of 10 °C). Printing passes of 25, 50, 75, and 100, respectively correspond to film thicknesses of 0.4, 0.75, 1.1, and 1.6 µm respectively.

ADVANCED
SCIENCE NEWS
www.advancedsciencenews.com

ADVANCED
ELECTRONIC
MATERIALS
www.advelectronicmat.de

FULL PAPER

BTNWs the trend is different; the electrical conductivity of the nitrogen-annealed BTNWs remains unchanged up to a thickness of 50 printer pass layers and then drops to nearly half of the conductivity with a film thickness of 25 printer pass layers. Thus, nitrogen annealing has minimal effect on the electrical conductivity of the BTNW films—a phenomenon that corroborates the lack of morphology changes in the BTNW nanowires and the slight deterioration of the crystallinity of the BTNWs upon nitrogen annealing as illustrated previously in Figures 2 and 3, respectively.

Thermal transport was also evaluated to assess the thermoelectric properties of the printed BTNW networks. Thermal transport was monitored by measuring the thermal diffusivity (characteristic time a phonon takes for the temperature to attain a steady state) of the BTNW networks with a transient electrothermal (TET) technique performed in a similar fashion to previous reports (see Section S4 in the Supporting Information for details).[34,35] A square pulse direct current is typically fed through the sample to induce joule heating in the network and the variation of voltage over the sample length is measured while the temperature evolves before reaching the steady state. This TET technique has been used to assess the thermal and electrical properties of wire/wire junctions in metallic NW networks;[36] however, no such study has been made in thermoelectric NW networks such as the printed BTNWs presented in this work. The temperature (T) change with time (t) is modeled following 1D heat transfer equation that involves thermal diffusivity as shown in Equation 1

$$\frac{\partial(\rho C_p T)}{\partial t} = k \frac{\partial^2 T}{\partial x^2} + q_0 \tag{1}$$

where ρ is the density, κ is the thermal conductivity, C_p is the heat capacity, and $\alpha = (\kappa/\rho \, C_p)$ is the intrinsic thermal diffusivity of the sample while q_0 is a constant relating to the electrical heating power per unit volume.[34] The theoretical solution to the above 1D thermal transport is given by[34]

$$T^* = \frac{96}{\pi^4} \sum_{m=1}^{\infty} \frac{1 - \exp(-(2m-1)^2 \pi^2 \alpha t / L^2)}{(2m-1)^4} \tag{2}$$

where α and L are the thermal diffusivity and length of sample, and t is time. Experimentally, the solution (T^*_{exp}) is acquired by obtaining the voltages in Equation 3
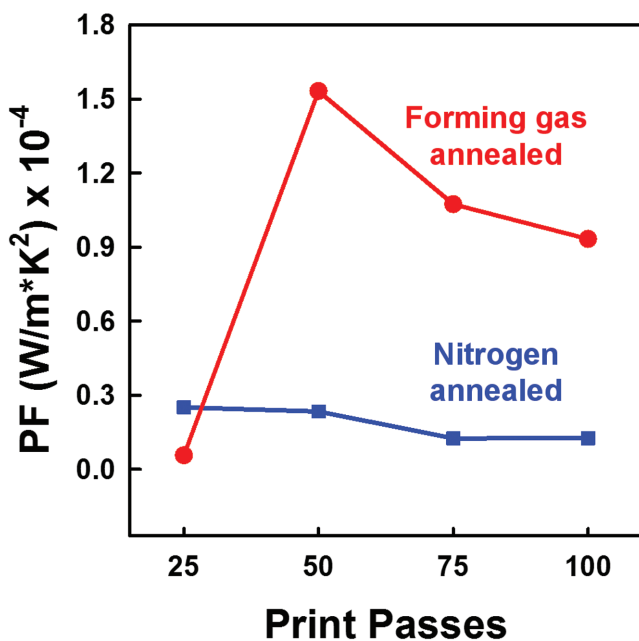
$$T^*_{exp} = \frac{V_{wire} - V_0}{V_1 - V_0} \tag{3}$$

where V_{wire} is the voltage evolution measured (in our case in an oscilloscope), V_1 is final voltage caused by joule heating (current induced), and V_0 is voltage before the pulse application. A fitting program developed was used to extract the thermal diffusivity data from theoretical and experimental analysis. The thermal diffusivity was evaluated for BTNWs annealed in both forming and nitrogen gas environments with different thicknesses (25, 50, 75, and 100 printer passes, respectively) (Figure 4a,c). All printed BTNW networks generally show a gradual decreasing trend in the thermal diffusivity with increasing film density/thickness. These measured

thermal diffusivity values fall within a range of 0.56–0.8 mm^2 s^{-1} for forming gas-annealed samples and 0.45–1.17 mm^2 s^{-1} for nitrogen-annealed samples.

Next the Seebeck coefficient, a measure of the thermoelectric sensitivity, was measured to further assess the thermoelectric efficiency of the printed BTNWs (see the details in the Experimental Section and Section S3 in the Supporting Information and results in Figure 4b,d). The Seebeck coefficient values for the printed BTNWs are negative, which is indicative of the dominant contribution of electron carriers that arise from Te-rich Bi_2Te_3 nanowires.[12] The magnitude of Seebeck coefficient is between 75 and 140 µV K^{-1} at room temperature. The distinctly annealed BTNW films show different temperature-dependent Seebeck coefficient trends. Printed BTNWs annealed with forming gas display an increasing (in negative direction) trend for Seebeck coefficient from room temperature to ≈140–170 °C, a constant trend between ≈140 and 170 °C, and a decreasing trend for temperatures above ≈170 °C. Films with nitrogen annealing, however, show constant and generally higher Seebeck coefficient values that sharply decrease after a temperature of ≈125 °C. Higher Seebeck values for nitrogen-annealed samples could be possible due to the higher carrier concentration. The increasing (in negative direction) Seebeck values from room temperature to ≈140 °C is indicative of degenerate semiconductor (semimetal) behavior. In the temperature regime between ≈140 and 170 °C, the excess hole contribution and electronic contribution to the transport remain balanced (with net negative and nearly constant Seebeck values) after which the contribution of hole substantially increases. The overall Seebeck values still remain electron dominated at 400 °C. Similar thermally induced hole-generation and hole-transport at temperatures beyond 125 °C is is displayed in all the BTNW films of distinct thickness and annealled n a nitrogen ambient. On the other hand, the relative stable value of the Seebeck coefficient in the nitrogen-annealed BTNW samples (annealing temperatures up to ≈125 °C) indicates the negligible influence nitrogen annealing has on the electronic properties of the BTNW samples at least at lower annealing temperatures. However, nitrogen annealing above temperatures of 125 °C induces a decrease in (electronic) Seebeck values which is indicative of the emergence of hole transport properties similar to BTNWs annealed in forming gas.

Finally, the room temperature power factor (PF = σS^2 where σ and S are electrical conductivity and Seebeck coefficient) was calculated to better assess the overall thermoelectric capability of the printed BTNW films (**Figure 5**). Once the thickness of the BTNW films reached 50 print passes or higher the disparity in the PF value between the distinctly annealed samples is significant (note that for low density/thickness BTNW films the electrical conductivity plays a more significant role than the Seebeck coefficient and resultant PF values for the printed BTNWs are low for both annealing scenarios). Thus although the room temperature Seebeck coefficient for nitrogen-annealed films is superior to those of the forming gas annealed ones, the overall product of electrical conductivity and the Seebeck coefficient, viz., the PF value, is higher. Subsequently, the resultant ZT value [$ZT = S^2\sigma T/k$ (where Z is the figure of merit, T is the absolute temperature, S is the Seebeck coefficient, and k is the total thermal conductivity)] of

ADVANCED
ELECTRONIC
MATERIALS
www.advelectronicmat.de

FULL PAPER

ADVANCED
SCIENCE NEWS
www.advancedsciencenews.com

Figure 5. Power factor of the printed BTNWs samples of varying thickness (i.e., 25, 50, 75, and 100 printer passes) annealed in a forming (red) and a nitrogen (blue) gas ambient.

the forming gas annealed printed BTNWs would also be higher; the forming gas annealed printed BTNWs will have a higher heat-to-electricity conversion. The obtained PF of 163 µW m^{-1} K^{-2} is higher than the previously reported PF of inkjet-printed Sb$_{1.5}$Bi$_{0.5}$Te$_3$ powders (116 µW m^{-1} K^{-2})[8] and dispenser printed Bi$_2$Te$_3$ powder (158 µW m^{-1} K^{-2}).[21] A room temperature figure of merit (or TE efficiency) of 0.26 and 0.05 was estimated for forming gas and nitrogen gas annealed BTNW films through the use of the equation $ZT = S^2\sigma T/k = (PF)T/(x\rho C_p\alpha)$, the calculated PF values, obtained diffusivity values for 50 print passes, an estimated 25% fill factor (x) of the wires, bulk Bi$_2$Te$_3$ density of 7.7 g cm^{-3} (ρ), and bulk Bi$_2$Te$_3$ heat capacity (C_p) of 124.65 J mol^{-1}.

3. Conclusions

In summary, for the first time a single crystalline Bi$_2$Te$_3$ nanowire ink has been formulated and inkjet printed. Structural, microstructural, electrical, thermal, and thermoelectric characterizations of the printed patterns were made to demonstrate its applications. The printed BTNW networks display a Seebeck coefficient up to 140 µV K^{-1}, which is on the same order of magnitude than BTNWs hot pressed into pellet form (≈200 µV K^{-1}), while the amount of Bi$_2$Te$_3$ used in the printed BTNWs is ≈1%–3% of the material that is used in their bulk counterparts.[12] This work demonstrates that inkjet printing of n-type telluride-based nanowires is possible and hence the subsequent fabrication of a printed thermoelectric generator (with both n-type and p-type elements/legs) should also be achievable. Other groups have developed techniques to inkjet print Bi$_2$Te$_3$ powders,[8,21] however, herein we report

for the first-time, inkjet printing of Bi$_2$Te$_3$ nanowires with an achieved high power factor (163 µW m^{-1} K^{-2}) and TE efficiency ($ZT ≈ 0.26$) at room temperature. Thus, this work helps to pave the way for the scalable roll-to-roll manufacturing of thin film, printed thermoelectrics.

4. Experimental Section

Nanowire Synthesis: TeO$_2$ powder (99.999%), potassium hydroxide, PVP, EG, hydrazine hydrate, and Bi(NO$_3$)$_3$.5H$_2$O were acquired from Sigma-Aldrich. The printable BTNW ink was created by first mixing 0.2 g of PVP, 0.6 g of KOH, and 0.4788 g of TeO$_2$ powder into a thermally insulated controlled three-neck glass flask that is heated to 160 °C and maintained at this temperature throughout the entire BTNW synthesis process. After 1 h of heating, ≈1 mL of hydrazine hydrate is injected into the solution to help reduce the TeO$_2$ and form tellurium nanowires. Next, a bismuth precursor solution is prepared by mixing 0.82 g of Bi(NO$_3$)$_3$.5H$_2$O into 5 mL of EG. This bismuth precursor solution is then added into the tellurium nanowire solution at 160 °C and after ≈1 h the final BTNWs can be extracted and further processed for printing.

Ink Formulation: To formulate the jettable ink, 5 mL of the liquid phase synthesized BTNWs are added to 10 mL of DI water. The mixture is then aliquoted and distributed into smaller Eppendorf tubes (1 mL of solution added to each tube) for subsequent centrifugation. The BTNWs are centrifuged at 10 000 rpm for 5 min, and the resultant supernatant solution is then removed. The BTNW pellet is then redispersed in DI water (1 mL of DI added to each tube and then vortexed on low settings), centrifuged again, and the resultant supernatant removed again. This washing process is repeated for three times in order to remove ethylene glycol, KOH, and hydrazine from the original BTNW stock solution. The sediment was collected and redispersed in DI water. Next, 2 h of water bath sonication was performed to well disperse the Bi$_2$Te$_3$ NWs in DI water. The resultant ink exhibited high stability and could be stored at 4 °C for 2 months without sedimentation.

Inkjet Printing of BTNWs: The glass printing substrates were cleaned with acetone, isopropanol, and methanol, respectively, and were then dried with nitrogen gas before use. To print the BTNWs onto the glass, 3 mL of the formulated ink was loaded into a printer cartridge that supplied a piezoelectric-controlled printer head with 16 nozzles of a Fujifilm Dimatix Materials Printer system (Model DMP-2831). Printer patterns were CAD designed in Solidworks and then converted into an equivalent printable bitmap file that is compatible with the software capabilities of the Dimatix Materials Printer. The glass substrates were secured to a heated vacuum platen maintained at a temperature of 50 °C during the heating process. Before printing, the voltage on each nozzle was modified (21–24 V) based on drop geometry visualized from the drop watcher while the number of printed layers (i.e., 25, 50, 75, and 100 single-print passes) was varied.

Annealing of Inkjet-Printed BTNWs: The printed BTNW samples were left on the heated vacuum platen (temperature of 50 °C) for an additional hour after printing to further remove/evaporate moisture. The printed BTNWs were subsequently annealed in a tubular furnace with two different recipes—recipe 1: annealing at 400 °C with forming gas flow (5% hydrogen in argon) for 2 h; and recipe 2: annealing at 400 °C with nitrogen gas flow for 2 h. To avoid atmospheric oxidation of NW surface, the samples were kept within a glove box after the annealing processes were completed.

Imaging and Thickness Measurements: FESEM images were measured using an FEI Quanta 250 in secondary electron mode using 10 kV accelerating voltage with the sample surface kept at ≈10 mm of working distance from the field emitter source aperture. An Oxfords Instruments Aztec X-Max 80 detector system connected to FEI Quanta 250 was used to collect the EDX photons for elemental detection. The thickness of all samples was measured using a surface profilometer and hence the number of printer passes correlated to the following thickness measurements: 25 print layers ≈0.4 µm thick, 50 print layers ≈0.75 µm thick, 75 print layers ≈1.1 µm thick, and 100 print layers ≈1.6 µm thick.

XRD Measurement: The XRD measurements are performed using a powder diffractometer (Model Rigaku's Ultima IV) with CuKα radiation ($\lambda \approx 1.5418$ Å). BTNWs printed on a glass slides were scanned from 10° to 70° at a scan rate of 0.02° s^{-1}.

Electrical Conductivity Measurements: The electrical conductivity was measured using a four-probe resistivity measurement setup (Jandel multi height probe with RM 3000 test unit). The outer two probes were used to send current into the structure while the inner two probes were used to read the potential difference. The room temperature electrical conductivity of the printed nanowire films was calculated in conjunction with the average thickness information previously measured.

Thermal Diffusivity Measurements: Thermal diffusivity was measured using a transient electrothermal technique reported earlier.[34] Briefly, samples printed with BTNWs were suspended in air and was held with silver paste between two copper electrodes. A direct electric current was passed through the sample to induce joule heating. The resulted voltage–time relationship was recorded by an oscilloscope. The data were then processed by predefined equations in MATLAB. It should also be noted that the BTNWs were printed on polyimide film and therefore the thermal diffusivity results contained a contribution from the polyimide (albeit small) in addition to the printed BTNWs. Also, the measurement results excluded any contribution originating from radiation (see Sections S4 and S5 in the Supporting Information).

Seebeck Coefficient Measurements: Seebeck coefficient measurements of all the printed samples were performed under vacuum using an LSR–3 Linseis–Seebeck coefficient and electric resistivity measurement unit. The printed pattern on glass substrate was first coated with silver paint at both the ends of the printed pattern in such a way that the silver contact spreads over the edges of the substrate. The sample was then vertically positioned between the two electrodes and a temperature gradient was applied across the sample as the electrodes serve as a heater and a heat sink (see the Supporting Information for the schematic of the measurement setup and the temperature gradient). The potential difference generated in their vicinity (with maximum temperature fluctuations within couple hundred of millikelvin and a voltage resolution of tens of nanovolts) was measured.

Supporting Information

Supporting Information is available from the Wiley Online Library or from the author.

Acknowledgements

[1] L. A. Fisk, *Science* **2005**, *309*, 2016.
[2] S. J. Kim, J. H. We, B. J. Cho, *Energy Environ. Sci.* **2014**, *7*, 1959.
[3] M. Hyland, H. Hunter, J. Liu, E. Veety, D. Vashaee, *Appl. Energy* **2016**, *182*, 518.
[4] G. J. Snyder, *Electrochem. Soc. Interface* **2008**, *17*, 54.
[5] A. Date, A. Date, C. Dixon, A. Akbarzadeh, *Renewable Sustainable Energy Rev.* **2014**, *33*, 371.
[6] D. M. Rowe, in *CRC Handbook of Thermoelectrics*, CRC Press, Boca Raton, Florida, United State, **1995**.
[7] J. Lee, H. J. Kim, L. Chen, S. H. Choi, G. N. Mathur, V. K. Varadan, *Proc. SPIE* **2013**, *8691*, 26.
[8] Z. Lu, M. Layani, X. Zhao, L. P. Tan, T. Sun, S. Fan, Q. Yan, S. Magdassi, H. H. Hng, *Small* **2014**, *10*, 3551.
[9] A. I. Hochbaum, R. Chen, R. D. Delgado, W. Liang, E. C. Garnett, M. Najarian, A. Majumdar, P. Yang, *Nature* **2008**, *451*, 163.
[10] L. Hicks, M. Dresselhaus, *Phys. Rev. B* **1993**, *47*, 16631.
[11] Y. Xia, P. Yang, Y. Sun, Y. Wu, B. Mayers, B. Gates, Y. Yin, F. Kim, H. Yan, *Adv. Mater.* **2003**, *15*, 353.
[12] G. Zhang, B. Kirk, L. A. Jauregui, H. Yang, X. Xu, Y. P. Chen, Y. Wu, *Nano Lett.* **2011**, *12*, 56.
[13] H. Yang, S. W. Finefrock, J. D. Albarracin Caballero, Y. Wu, *J. Am. Chem. Soc.* **2014**, *136*, 10242.
[14] S. W. Finefrock, H. Fang, H. Yang, H. Darsono, Y. Wu, *Nanoscale* **2014**, *6*, 7872.
[15] B. Hamdou, J. Gooth, A. Dorn, E. Pippel, K. Nielsch, *Appl. Phys. Lett.* **2013**, *103*, 193107.
[16] Z.-G. Chen, G. Han, L. Yang, L. Cheng, J. Zou, *Prog. Nat. Sci.: Mater. Int.* **2012**, *22*, 535.
[17] J. A. Lee, A. E. Aliev, J. S. Bykova, M. J. de Andrade, D. Kim, H. J. Sim, X. Lepró, A. A. Zakhidov, J. B. Lee, G. M. Spinks, *Adv. Mater.* **2016**, *28*, 5038.
[18] J. H. We, S. J. Kim, G. S. Kim, B. J. Cho, *J. Alloys Compd.* **2013**, *552*, 107.
[19] Z. Cao, E. Koukharenko, M. Tudor, R. Torah, S. Beeby, *J. Phys.: Conf. Ser.* **2013**, *476*, 012031.
[20] D. Madan, A. Chen, P. K. Wright, J. W. Evans, *J. Appl. Phys.* **2011**, *109*, 034904.
[21] A. Chen, D. Madan, P. Wright, J. Evans, *J. Micromech. Microeng.* **2011**, *21*, 104006.
[22] Y. Yang, Z.-H. Lin, T. Hou, F. Zhang, Z. L. Wang, *Nano Res.* **2012**, *5*, 888.
[23] L. Fonseca, J.-D. Santos, A. Roncaglia, D. Narducci, C. Calaza, M. Salleras, I. Donmez, A. Tarancon, A. Morata, G. Gadea, *Semicond. Sci. Technol.* **2016**, *31*, 084001.
[24] S. R. Das, Q. Nian, A. A. Cargill, J. A. Hondred, S. Ding, M. Saei, G. J. Cheng, J. C. Claussen, *Nanoscale* **2016**, *8*, 15870.
[25] P. Maisch, K. C. Tam, L. Lucera, H.-J. Egelhaaf, H. Scheiber, E. Maier, C. J. Brabec, *Org. Electron.* **2016**, *38*, 139.
[26] S. G. Hashmi, M. Ozkan, J. Halme, S. M. Zakeeruddin, J. Paltakari, M. Gratzel, P. D. Lund, *Energy Environ. Sci.* **2016**, *9*, 2453.
[27] K.-H. Choi, J. Yoo, C. K. Lee, S.-Y. Lee, *Energy Environ. Sci.* **2016**, *9*, 2812.
[28] M. Engel, J. P. Small, M. Steiner, M. Freitag, A. A. Green, M. C. Hersam, P. Avouris, *ACS Nano* **2008**, *2*, 2445.
[29] L. Hu, D. Hecht, G. Grüner, *Nano Lett.* **2004**, *4*, 2513.
[30] R. Chen, S. R. Das, C. Jeong, M. R. Khan, D. B. Janes, M. A. Alam, *Adv. Funct. Mater.* **2013**, *23*, 5150.
[31] P. Serre, M. Mongillo, P. Periwal, T. Baron, C. Ternon, *Nanotechnology* **2014**, *26*, 015201.
[32] D.-m. Sun, M. Y. Timmermans, Y. Tian, A. G. Nasibulin, E. I. Kauppinen, S. Kishimoto, T. Mizutani, Y. Ohno, *Nat. Nanotechnol.* **2011**, *6*, 156.
[33] D. J. Finn, M. Lotya, J. N. Coleman, *ACS Appl. Mater. Interfaces* **2015**, *7*, 9254.
[34] J. Guo, X. Wang, T. Wang, *J. Appl. Phys.* **2007**, *101*, 063537.
[35] H. Lin, S. Xu, X. Wang, N. Mei, *Small* **2013**, *9*, 2585.
[36] Z. Cheng, M. Han, P. Yuan, S. Xu, B. A. Cola, X. Wang, *RSC Adv.*, **2016**, *6*, 90674.